Revision 1

Effects of composition and pressure on electronic states of iron in bridgmanite

Susannah M. Dorfman[1,2], Vasily Potapkin[3], Mingda Lv[1], Eran Greenberg[4,*], Ilya Kupenko[3,5], Aleksandr I. Chumakov[5], Wenli Bi[6,7], E. Ercan Alp[6], Jiachao Liu[1], Arnaud Magrez[8], Siân E. Dutton[9,†], Robert J. Cava[9], Catherine A. McCammon[10], Philippe Gillet[2]

1: Department of Earth and Environmental Sciences, Michigan State University, East Lansing, MI, USA.

2: Earth and Planetary Science Laboratory, Institute of Physics, École Polytechnique Fédérale de Lausanne, CH-1015 Lausanne, Switzerland.

3: Institute of Mineralogy, University of Münster, Münster, Germany.

4: School of Physics & Astronomy, Tel-Aviv University, Tel-Aviv, Israel.

5: ESRF-The European Synchrotron, 71, Avenue des Martyrs, Grenoble, France.

6: Advanced Photon Source, Argonne National Laboratory, Argonne, Illinois 60439, USA.

7: Department of Geology, University of Illinois at Urbana-Champaign, Urbana, Illinois 61801, USA; Department of Physics, University of Alabama at Birmingham, Birmingham, Alabama 35294, USA.

8: Crystal Growth Facility, Institute of Physics, École Polytechnique Fédérale de Lausanne, CH-1015 Lausanne, Switzerland.

9: Department of Chemistry, Princeton University, Princeton, NJ, USA.

10: Bayerisches Geoinstitut, University of Bayreuth, Bayreuth, Germany.

*now at Applied Physics Department, Soreq Nuclear Research Center (NRC), Yavne 81800, Israel.

†now at Cavendish Laboratory, University of Cambridge, Cambridge, CB3 OHE, UK.

Abstract

Electronic states of iron in the lower mantle's dominant mineral, $(Mg,Fe,Al)(Fe,Al,Si)O_3$ bridgmanite, control physical properties of the mantle including density, elasticity, and electrical and thermal conductivity. However, determination of electronic states of iron has been controversial, in part due to different interpretations of Mössbauer spectroscopy results used to identify spin state, valence state, and site occupancy of iron. We applied energy-domain Mössbauer spectroscopy to a set of four bridgmanite samples spanning a wide range of compositions: 10-50% Fe/total cations, 0-25% Al/total cations, 12-100% Fe^{3+}/total Fe. Measurements performed in the diamond anvil cell at pressures up to 76 GPa below and above the high to low spin transition in Fe^{3+} provide a Mössbauer reference library for bridgmanite and demonstrate the effects of pressure and composition on electronic states of iron. Results indicate that although the spin transition in Fe^{3+} in the bridgmanite B-site occurs as predicted, it does not strongly affect the observed quadrupole splitting of 1.4 mm/s, and only decreases center shift for this site to 0 mm/s at ~70 GPa. Thus center shift can easily distinguish Fe^{3+} from Fe^{2+} at high pressure, which exhibits two distinct Mössbauer sites with center shift ~1 mm/s and quadrupole splitting 2.4-3.1 and 3.9 mm/s at ~70 GPa. Correct quantification of Fe^{3+}/total Fe in bridgmanite

is required to constrain effects of composition and redox states in experimental measurements of seismic properties of bridgmanite. In Fe-rich, mixed-valence bridgmanite at deep-mantle-relevant pressures, up to ~20% of the Fe may be a $Fe^{2.5+}$ charge transfer component, which should enhance electrical and thermal conductivity in Fe-rich heterogeneities at the base of Earth's mantle.

Keywords: bridgmanite, Mössbauer spectroscopy, iron oxidation state, lower mantle

Introduction

Iron-bearing bridgmanite, the most abundant material in the Earth's interior, is the dominant mineral responsible for chemical and physical behavior of the lower mantle. Redox of iron in bridgmanite buffers the mantle and thus has implications for formation of the atmosphere and habitability of the planet, storage and transport of volatiles including water and carbon in the deep interior, and interpretation of structures and dynamic processes observed by seismic tomography (e.g. Frost and McCammon 2008; Gu et al. 2016; Liu et al. 2018). Heterogeneous structures at the base of the mantle including large low shear velocity provinces and ultra-low velocity zones have been suggested to be iron-rich relative to surrounding mantle based on inversion of normal mode data (Ishii and Tromp 1999), tidal tomography (Lau et al. 2017), and travel times of seismic waves reflected off the core-mantle boundary (Rost et al. 2005); identifying these features and their role in the differentiation and mixing of the mantle depends on accurate constraints on the physical properties of iron-rich bridgmanite. Because bridgmanite samples from the lower mantle have not been recovered, redox conditions are inferred based on

remote geophysical observations and experimental and theoretical modeling of chemistry at extreme pressures and temperatures.

Depth and composition both affect redox states of iron incorporated in the mantle's dominant phase, but efforts to measure these changes have been complicated by the crystal chemistry of $(Mg,Fe,Al)(Fe,Al,Si)O_3$ bridgmanite (e.g. McCammon et al. 2013; Shim et al. 2017). Bridgmanite adopts the orthorhombic $GdFeO_3$-type perovskite structure, with a larger 8-12-fold pseudo-dodecahedral "A" site and smaller 6-fold octahedral "B" site. Both Fe^{2+} and Fe^{3+} substitute for Mg in the A-site, while only the smaller Fe^{3+} ion may substitute for Si in the B-site. At pressure/temperature conditions corresponding to the top of the lower mantle, bridgmanite typically exhibits Fe^{3+}/total Fe ratio at least 50%, even under reducing conditions in contact with metallic iron (Frost et al. 2004; Shim et al. 2017). The Fe^{3+}/total Fe ratio in bridgmanite synthesized at pressures corresponding to the deep lower mantle has been observed to decrease with pressure to ~15%, then increase again to ~50% (Shim et al. 2017). Variations in valence states of iron with depth are inferred to be due to energetics of substitution mechanisms as local structure and spin state of iron change with depth. Distortion of the perovskite structure due to pressure and/or composition divides the A-site into A1- and A2-sites (Hsu et al. 2010; Hummer and Fei 2012) and occurs at similar conditions as the observed decrease in Fe^{3+}/total Fe. A spin-pairing transition in Fe^{3+} in the B-site at ~48 GPa, corresponding to the mid-lower-mantle, may also drive partitioning of Fe^{3+} into the B-site (Badro et al. 2004; Catalli et al. 2010, 2011; Hsu et al. 2011; Liu et al. 2018). The presence of Al may also modify incorporation of Fe^{3+} in bridgmanite through paired substitution of trivalent cations for Mg and Si (e.g. Frost and Langenhorst 2002; Piet et al. 2016) and formation of vacancies in cation (Sinmyo et al. 2014;

Kupenko et al. 2015) or oxygen sites (Grüninger et al. 2019; Liu et al. 2019). Based on experiments (e.g. Potapkin et al. 2013) and computational modeling using density functional theory (DFT) (Caracas 2010), paired substitution places Al in the B-site and Fe^{3+} in the A-site at equilibrium, though some observations support migration of Al and Fe^{3+} between the two sites (Catalli et al. 2011) and/or migration of Fe^{3+} from A to B site due to vacancy redistribution (Kupenko et al. 2015). In bridgmanite compositions with mixed valence states, Fe^{2+}–Fe^{3+} electronic charge transfer may also create $Fe^{2.5+}$ states (Mattson and Rossman 1987, Burns 1993). Because the separation distance between A and B sites is smaller than between A and adjacent A sites, the activation energy related to the distance of electron migration was suggested to be lower for A-B Fe^{2+}–Fe^{3+} charge transfer (Fei et al. 1994). For the same reason, charge transfer is generally expected to be promoted by pressure and impeded by temperature (Mattson and Rossman 1987; Fei et al. 1994; Xu and McCammon 2002; Lobanov et al. 2017). In total, Fe in bridgmanite in Earth's mantle may be distributed among a multitude of different combinations of valence state (Fe^{2+}, $Fe^{2.5+}$, Fe^{3+}), crystallographic site (A1, A2, or B), and spin state (high or low).

Controversy over the electronic states of iron in bridgmanite has also been drawn out by different interpretations of a key observational technique, Mössbauer spectroscopy. The Mössbauer effect allows each valence state, coordination environment, and spin state to be distinguished by characteristic values for center shift (CS) and quadrupole splitting (QS) (Dyar et al. 2006). Interpretation of CS and QS obtained at high pressures requires deconvolving poorly-constrained effects of structural and electronic changes. Pressure generally distorts crystallographic sites of bridgmanite, leading to higher QS with pressure (e.g. Lin et al. 2013; McCammon et al. 2013).

Although the existence of the spin transition in Fe^{3+} in the bridgmanite B-site is now well-accepted (Lin et al. 2013; Badro 2014), the published values for Mössbauer parameters of low-spin Fe^{3+} in bridgmanite range from CS~1 mm/s and QS ~3 mm/s similar to high-spin Fe^{2+} (Catalli et al. 2010; Gu et al. 2012) to CS<0.5 mm/s and QS ~1-1.5 mm/s similar to high-spin Fe^{3+} (Jackson et al. 2005; Kupenko et al. 2015; Liu et al. 2018). Predictions by DFT support higher QS values 2-3 mm/s due to asymmetrical electronic field gradient generated by spin-down electrons in the B-site, but have not addressed CS of low-spin Fe^{3+} (Hsu et al. 2011). Depending on which of these interpretations is correct, low-spin Fe^{3+} may be misidentified as high-spin Fe^{2+} or high-spin Fe^{3+}, or vice versa. The conditions at which the spin transition is reported based on these observations range from 13-24 GPa (Mao et al. 2015) to 50-70 GPa (Catalli et al. 2010, 2011). Other phenomena suggested to impact Mössbauer spectra of bridgmanite and related compounds at high pressures include charge-transfer, which should result in enhanced electrical and thermal conductivity in silicates/perovskites with a mixture of Fe^{2+} and Fe^{3+} (Fei et al. 1994; Xu and McCammon 2002; Keppler et al. 2008; Long et al. 2009), and changes in glasses in recoil-free fraction of Fe^{2+} and Fe^{3+}, causing shifts in the relative contributions of Fe^{2+} and Fe^{3+} to spectral area (Prescher et al. 2014). In addition, spectra for complex materials such as bridgmanite suffer from overlapping peaks and non-unique fitting. These issues may be addressed by complementary techniques such as X-ray emission spectroscopy and X-ray diffraction to independently constrain spin state and structure (e.g. Catalli et al. 2010) and systematic analysis of a range of compositions (e.g. McCammon et al. 2013).

Previous attempts to prepare well-characterized bridgmanite rely on samples synthesized in the multianvil press, which is typically limited to ~25 GPa. At these conditions, bridgmanite is stable

with only up to ~15-20% Fe (Fei et al. 1996; Tange et al. 2009), and typically exhibits a mixture of Fe^{2+} and Fe^{3+} depending on composition and f_{O2} (e.g. Frost and Langenhorst 2002; Frost et al. 2004). At pressures ~75-100 GPa in the diamond anvil cell, a wider range of compositions with up to at least 75-90% $FeSiO_3$ and lower Fe^{3+}/total Fe becomes stable (Tateno et al. 2007; Dorfman et al. 2012, 2013; Ismailova et al. 2016). The goal of this study is to systematically analyze electronic states of iron-rich bridgmanite using Mössbauer spectroscopy of well-characterized end-member samples. These experiments resolve discrepancies in interpretation of high-pressure Mössbauer spectra of bridgmanite by firmly constraining valence states of iron at 1 bar, where Mössbauer parameters CS and QS are unambiguous. Results address the conditions and observable characteristics of possible spin transitions and charge transfer, and will be important to future characterization of bridgmanite relevant to Earth's deep mantle heterogeneities.

Methods

Four bridgmanite compositions were examined ranging from 12-100% Fe^{3+}/total Fe and from 10-50% Fe/total cations. Bridgmanites were synthesized from the following starting materials:

- 50% enstatite, 50% ferrosilite (En50Fs50) pigeonite was synthesized at the Crystal Growth Facility at EPFL in a gas-mixing furnace. A stoichiometric mixture of Fe_2O_3 (enriched to 48.3% ^{57}Fe), MgO and SiO_2 was ground in an agate mortar until homogenous and cold-sintered in a 3-ton press at room temperature for 1 minute. The resulting pellet was placed in an alumina crucible on a bed of unenriched powder mixture of the same composition. The sample was first heated in air at 1000°C, then reduced

147 under an N_2/H_2 mixture bubbled through H_2O at 1100°-1200°C for 3 days, then rapidly
148 quenched to room temperature. Mössbauer analysis of the starting material was consistent
149 with complete reduction of ferric iron to ferrous iron, with a detection limit of a few
150 percent. X-ray diffraction and electron microprobe analysis (Table 1) confirmed that the
151 oxides transformed to monoclinic *P2₁/c* pigeonite with composition $(Mg_{0.52}Fe^{2+}_{0.48})SiO_3$
152 (0% ferric before bridgmanite synthesis).

153 • 90% enstatite, 10% hematite (En90Hem10) glass starting material was synthesized from
154 intimately mixed Fe_2O_3 (enriched to 96.6% ^{57}Fe), MgO and SiO_2 powders by
155 containerless laser-levitation (Weber et al. 1994) under compressed air at IPGP, Paris.
156 Mössbauer spectroscopy indicates total ferric iron content of the glass before bridgmanite
157 synthesis is ~30%. The homogeneity and composition of the glass were determined by
158 electron microprobe analysis (Table 1), yielding formula for this sample as follows:
159 $Mg_{0.97}Fe^{2+}_{0.14}Fe^{3+}_{0.06}Si_{0.90}O_3$. Oxygen deficiency in measured formula may be due to use
160 of Fe^{2+}-rich standards and few-% uncertainty indicated by 97-98% oxide totals during
161 microprobe measurements.

162 • 50% enstatite, 50% hematite (En50Hem50) akimotoite synthesis and characterization
163 were described in (Liu et al. 2018). Based on microprobe analysis and Mössbauer
164 spectroscopy, the formula obtained for this sample is $Mg_{0.46}Fe^{3+}_{1.04}Si_{0.49}O_3$ (100% ferric).

165 • 75% ferrosilite, 25% corundum (Fs75Co25, or almandine-composition) glass synthesis
166 and characterization were described in Dorfman et al. (2016). The composition of the
167 glass, normalized to 3 oxygens, is $Fe^{2+}_{0.55}Fe^{3+}_{0.12}Al_{0.54}Si_{0.73}O_3$ (20% ferric before
168 bridgmanite synthesis).

Starting materials were loaded as crystalline powder or glass chip in diamond anvil cells with 100-150-micrometer culet and 300-micrometer bevel. Each sample was contained in a 30-50-micrometer hole drilled in a Re gasket. To insulate the samples during laser heating and transmit quasi-hydrostatic stress, En50Fs50 and Fs75Co25 were loaded sandwiched between platelets of NaCl; En90Hem10 was loaded in Ar gas at the EPFL; and En50Hem50 was loaded in Ne gas using the COMPRES/GSECARS gas loading system (Rivers et al. 2008). Pressure during experiments up to ~100 GPa was measured by Raman spectroscopy of the stressed diamond anvil culet center (Akahama and Kawamura 2006), or for En50Hem50 a ruby sphere loaded with the sample (Mao et al. 1986).

Bridgmanite was synthesized from Fs75Co25, En50Fs50, and En90Hem10 compositions as in previous studies (Dorfman et al. 2012, 2013) by laser heating to 2000-2500 K for ~20-60 min after compression at 300 K directly to ~75-100 GPa. The transformation and homogeneity of each sample was confirmed by X-ray diffraction at beamlines ID27 and ID09 (λ=0.3738 Å and 0.4117 Å or 0.4155 Å, respectively) of the ESRF (Figure 1). Minor $CaCl_2$-type SiO_2 diffraction peaks are also observed in some samples after laser heating. As described by Liu et al. (2018), the En50Hem50 akimotoite starting material transforms reproducibly and reversibly to bridgmanite at 300 K and 22-26 GPa, so this sample was simply compressed at 300 K.

Energy-domain Mössbauer spectroscopy was performed at the Nuclear Resonance beamline ID18 of the European Synchrotron Radiation Facility (Rüffer and Chumakov 1996; Potapkin et al. 2012) and the COMPRES/sector 3 offline Mössbauer spectroscopy laboratory at the Advanced Photon Source at Argonne National Laboratory. At ID18, incident light is synchrotron X-rays monochromatized by a $^{57}FeBO_3$ single crystal to the ^{57}Fe resonant energy of 14.4 keV

with energy resolution of ~5.5 neV. The X-ray beam is focused to ~9x14 micrometers full width at half maximum. At the sector 3 offline Mössbauer laboratory, incident gamma-rays are provided by a 400-micrometer-diameter radioactive ^{57}Co point source. To generate a range of energies for absorption spectroscopy measurements, both the $^{57}FeBO_3$ monochromator at ID18 and the ^{57}Co at sector 3 are oscillated +/- 5mm/s (1 bar measurement at sector 3 used +/- 10 mm/s). Source velocities are calibrated with an α-Fe foil standard at 300 K. Synchrotron source line width and center shift are calibrated with a $K_2Mg^{57}Fe(CN)_6$ standard before and after each measurement. The linewidth for the conventional measurements was set to match a 6-month-old radioactive point source. Synchrotron Mössbauer spectra were collected for ~2-8 hrs at each pressure. Conventional Mössbauer spectra were obtained for ~2 weeks each. Spectra were fit to pseudo Voigt doublets using MossA software (Prescher et al. 2012). All spectra were fit using a full transmission integral to account for thicknesses of radiation sources and samples.

Results and discussion

To ensure no change in valence states of Fe across the measured pressure range, all Mössbauer spectroscopy measurements were performed at 300 K and no additional heating was applied to samples after synthesis of bridgmanite. Upon laser heating, both structural transformation and redox may occur. Although some previous studies assume Fe^{3+}/total Fe does not change during synthesis (e.g. Nishio-Hamane et al. 2007; Lundin et al. 2008; Dorfman et al. 2013), redox during laser heating is confirmed by our data to result in differences in Fe^{3+}/total Fe in synthesized bridgmanite relative to starting materials. During 300 K compression and decompression, we assume that kinetics do not permit site-site diffusion and redox reactions. Therefore, Fe^{3+}/total Fe for bridgmanites synthesized at high pressure may be fixed to values

observed after 300 K decompression to 1 bar (these Fe^{3+}/total Fe values are reported here in figures and tables). Mössbauer spectra were measured for Fs75Co25, En50Fs50, and En90Hem10 bridgmanites on decompression from ~75-100 GPa in ~25 GPa steps to 1 bar (Figures 2-4 a-c). En50Hem50 akimotoite was observed upon compression from 1 bar to bridgmanite at 32 and 70 GPa (Figures 2-4 d). Changes in the Mössbauer parameters of each bridgmanite composition during 300 K compression/decompression (Table 2, Figure 5) may be due to 1) electronic spin transitions, 2) pressure-induced structural changes including site distortion or amorphization, or 3) charge transfer between nearby Fe ions.

The spin transition in Fe^{3+}

Effects of the high-to-low spin transition on Mössbauer parameters of Fe^{3+} in bridgmanite may be clearly observed in En50Hem50 bridgmanite, for which the spin transition in the octahedral site has been documented at ~48 GPa at 300 K by X-ray diffraction and X-ray emission spectroscopy (Liu et al. 2018). En50Hem50 bridgmanite is 100% Fe^{3+}, with 50% Fe in the pseudo-dodecahedral site, and 50% Fe in the octahedral site. Mössbauer spectra at high pressure exhibit two closely-overlapping doublets, with absorption at ~-0.4-0.0 mm/s and ~0.6-1 mm/s (Figure 3d, Figure 4d). Across the pressure-induced spin transition from 32 to 70 GPa, spectra change slightly: average CS decreases by 0.15 mm/s and QS increases by 0.35 mm/s. Two reasonable fits to these data are possible for a sample with pure Fe^{3+}: either Fe^{3+} in A- and B-sites adopt CS differing by <0.05 mm/s with contrasting QS, 0.6-0.9 and 1.4-1.8 mm/s, or the difference in CS is larger, ~0.4 mm/s, while QS is identical within ~0.5 mm/s. Neither option is consistent with a large change across the spin transition to QS ~3 mm/s predicted in bridgmanite by DFT (Hsu et al. 2011). At 32 GPa (Figure 3d), the fit with contrasting CS would produce

CS=0.45 mm/s for the higher CS component, which would be high for Fe^{3+} (Figure 5). We therefore favor a fit with contrasting QS for high-spin Fe^{3+} in A-site vs. B-site, consistent with the different asymmetry of the two sites in high-spin state. At 70 GPa (Figure 4d), the overall decrease in CS allows a fit with contrasting CS with acceptable Mössbauer parameters for Fe^{3+} for both sites, where the low-spin B-site Fe^{3+} exhibits lower CS and higher QS relative to high-spin B-site Fe^{3+} at lower pressure. In addition, recent data for well-characterized samples indicate that pressure tends to increase QS (i.e. level of structural distortion around the iron ion increases), and the principal change in Mössbauer parameters of octahedrally-coordinated Fe^{3+} across the spin transition is a decrease in CS (i.e. density of electrons around the iron nucleus increases) (Pasternak et al. 2002; Kupenko et al. 2015; Liu et al. 2018) (Table 3). We thus obtain CS ~0.35 mm/s for high-spin Fe^{3+} in both sites at 32 GPa below the spin transition, and a lower CS -0.07 mm/s for low-spin Fe^{3+} at 70 GPa (Table 2, Figure 5).

These results can be used to determine whether spin transitions occur in other compositions with mixed valence states of iron. For less Fe^{3+}-rich En50Fs50 and En90Hem10 compositions, Fe^{3+} doublets can be interpreted based on values observed at similar conditions for En50Hem50. The fit uncertainty for Fe^{3+} doublets in En50Fs50 at 75 GPa is large (as much as ~1 mm/s) due to overlap with other doublets, but the refined value 0.4 mm/s is consistent with high-spin Fe^{3+} in the A-site, as expected with a (Mg+Fe)/Si ratio ~1 and B-site filled with Si. For En90Hem10, with ~50% Fe^{3+}, stronger, better-resolved Fe^{3+} exhibits a slight decrease in CS, from 0.34 mm/s to 0.29 mm/s at 36 and 67 GPa, respectively. While this CS indicates a dominantly HS Fe^{3+} component, based on an assumption of linear mixing of CS values as much as ~20% of the Fe^{3+} (~10% total Fe) may be low-spin Fe^{3+} in the B-site at 67 GPa (Figure 6a). This partial spin

transition is consistent with the more Si-depleted composition with space available for Fe^{3+} in the B-site.

Site distortion

All Fe^{2+}-bearing bridgmanite compositions exhibit splitting at lower-mantle pressures consistent with predictions of distortion of the A-site (Hsu et al. 2010). At pressures above 1 bar for Fe^{2+}-rich Fs75Co25 and En50Fs50 compositions, absorption at ~2-3 mm/s requires two Fe^{2+} sites (Figure 3a,b, Figure 4a,b). QS of both sites increases with pressure (Figure 5) and the relative weight of the higher-QS site increases, in accord with increasingly asymmetric A-sites. At ~75 GPa in these compositions, ~1/3 of the Fe^{2+} sites exhibit QS=3.8-3.9 mm/s, with the remaining Fe^{2+} at QS=2.1-2.5 mm/s. For Fe^{3+} in the A-site, QS remains relatively constant with pressure. However, spectral resolution does not allow us to either confirm or disprove development of multiple Fe^{3+} A-sites due to site distortion (Hummer and Fei 2012).

Charge transfer ($Fe^{2.5+}$)

The signature of charge transfer, i.e. increased delocalization of electrons between iron ions, is observed in Fe compositions Fs75Co25 and En50Fs50 as an absorption peak at ~1.6 mm/s (Figure 2a, Figure 3a, Figure 4a-b). This peak can be fitted with a doublet with CS ~0.8 and QS ~1.6, intermediate between typical parameters observed for Fe^{2+} and Fe^{3+} and similar to $Fe^{2.5+}$ as previously identified in bridgmanite (Fei et al. 1994; Xu and McCammon 2002) (Figure 7). The $Fe^{2.5+}$ doublet intensity is interpreted to represent 50% Fe^{2+} and 50% Fe^{3+} when calculating Fe^{3+}/total Fe (Figure 6b). This assumption yields constant Fe^{3+}/total Fe with 300 K compression/decompression for all compositions within ~10% error entailed in fitting site weights, indicating no change in total redox state with pressure.

In general, the favorability of charge transfer would be expected to depend on whether Fe^{2+} and Fe^{3+} occupy neighboring sites (note that Fe-rich En50Hem50 does not exhibit charge transfer because all Fe is Fe^{3+}) and how much energy is required for electrons to hop between these sites. As noted in previous work (Fei et al. 1994), the shortest site-site distances for electron migration in the bridgmanite structure are between face-sharing B-sites and A-sites. However, the iron-rich compositions examined in this study incorporate at least enough Al and Si to fill the B-site, and are expected to accommodate both Fe^{2+} and Fe^{3+} in the A-site. The face-sharing A-A site distance in Fe-rich bridgmanite, based on lattice parameters determined by X-ray diffraction (Dorfman et al. 2012, 2013), is ~10% larger than the face-sharing A-B site distance, but comparable to edge-sharing octahedra in chain silicates at 1 bar known to exhibit Fe^{2+}-Fe^{3+} charge transfer (Mattson and Rossman 1987).

In the Fs75Co25 composition, $Fe^{2.5+}$ completely replaces Fe^{3+} at all pressures at 300 K. Even at 1 bar, ~20% of the spectral weight is a component with CS=0.6 mm/s, too high for Fe^{3+} and consistent with $Fe^{2.5+}$ (Figure 7). With increasing pressure, the intensity of the $Fe^{2.5+}$ component is constant within uncertainty, though the Mössbauer parameters are more uncertain due to overlap. Rietveld refinement of atomic positions (Dorfman et al. 2012) confirms that all Fe in this composition resides in the A-site. As a result, charge transfer in this composition must take place between face-sharing A-site Fe^{2+} and A-site Fe^{3+}.

For En50Fs50-composition bridgmanite, Fe^{2+}-Fe^{3+} neighboring A-sites will be diluted by Mg in the A-site, and charge transfer appears to be possible but less favorable. A charge transfer component accounting for ~1/3 of the Fe^{3+} is needed to fit data obtained at ~75 GPa (Figure 4b). Although Fe^{2+}-Fe^{3+} neighboring A-sites would be expected to be nearly as common in En50Fs50

as in Fs75Co25, a separate Fe^{3+} doublet is still observed, and upon decompression to pressures 25 GPa and below the $Fe^{2.5+}$ component disappears (Figure 3a,b). Weights of $Fe^{2.5+}$ and Fe^{3+} sites at all conditions are consistent with the 1 bar Fe^{3+}/total Fe (Figure 6b). These observations suggest a pressure-driven crossover in the stability of charge transfer in this composition. Compression of adjoining sites is expected to lower energy required for electron transfer (Fei et al. 1994; Xu and McCammon 2002). The mobility of electrons between A-sites appears to increase accordingly between 25 and 75 GPa. Observations of charge transfer in En50Fs50 relative to Fs75Co25 bridgmanite these samples indicate that charge transfer is promoted by pressure and high Fe concentration.

Evidence for charge transfer in En90Hem10-composition bridgmanite, which is also mixed-valence but relatively Fe-poor and has (Mg+Fe)/(Al+Si) ratio greater than 1, is not clear (Figure 4c). A Fe^{2+} site with CS~0.8 at high pressures is observed in En90Hem10 composition, but broad peaks, high QS, and no change in intensity of Fe^{3+} doublets when this doublet appears (Figure 6b, Table 2) all suggest the CS 0.8 mm/s doublet is more likely to represent Fe^{2+} in untransformed glass starting material. In contrast to the Fe^{2+}-rich compositions Fs75Co25 and En50Fs50, in the En90Hem10 composition the ~50% Fe^{2+} and 50% Fe^{3+} are expected to occupy the A- and B-sites respectively due to the higher (Mg+Fe)/(Al+Si) ratio, so charge transfer would take place between A- and B-sites rather than two A-sites. Even for this lower Fe concentration, Fe^{2+}-Fe^{3+} neighboring sites would be expected to be common: the probability that none of the 8 B-sites surrounding Fe^{2+} in the A-site is Fe^{3+} should be ~50%. Under these conditions A-B site charge transfer is not evident, though the presence of an overlapping $Fe^{2.5+}$ doublet cannot be ruled out. In contrast to intuition based on electron migration distance (Fei et al. 1994), charge

transfer appears to be more favorable between face-sharing A-sites than between face-sharing A- and B-sites. Although the distance between A-sites is longer, the enthalpy cost of moving an electron into the highly-compressed B-site (effectively, Fe^{2+} in B and Fe^{3+} in A) may provide an explanation for a failure to observe A-B charge transfer.

Implications

If previous studies of physical properties of bridgmanite have misidentified or missed spin transitions based on incorrect assignment of sites observed by Mössbauer spectroscopy, predicted seismic velocities for iron-bearing lower mantle phase assemblages may be systematically offset. The greatest effects of valence states of iron on geophysical properties are likely to be observed in the shallow lower mantle due to softening during the spin transition for Fe^{3+}-bearing compositions (Shukla et al. 2016) and higher contrast in bulk compressibility and density between Fe^{2+}- and Fe^{3+}-rich bridgmanite at pressures at and below the Fe^{3+} spin transition (Liu et al. 2018). At greater depths above the spin transition pressure range, seismic velocities of Fe^{2+}- and Fe^{3+}-rich bridgmanite converge. While speciation of Fe will also affect partitioning of Fe between bridgmanite and ferropericlase in the mantle (e.g. Piet et al. 2016), the net effect of multiple orders of magnitude difference in bridgmanite-ferropericlase partition coefficient on density contrast is only 0.1% (Ricolleau et al. 2009; Dorfman and Duffy 2014), suggesting that effects of partitioning on elastic properties are too subtle to be observed via seismology. Attempts to use seismology to map the redox conditions of the lower mantle should focus on depths below the spin transition pressure, between 660 and 1000 km.

The dependence of charge transfer in mantle bridgmanite on composition and pressure may not significantly affect elastic properties, but could result in regional- and depth-variation of transport properties including electrical and thermal conductivity. A-A site charge transfer should have no effect on density of the bridgmanite structure as the overall site occupancy remains the same. A-B site charge transfer would decrease density by expanding the B-site, but based on our data, we infer that this mechanism is not significant in Earth's mantle. Either mechanism of charge transfer, along with other mechanisms including conductivity of vacancies and ions, will contribute to electrical and thermal conductivity (Xu and McCammon 2002). Our observations do support enhancement of charge transfer by Fe-enrichment and high pressures corresponding to the deep lower mantle—both likely characteristics of dense heterogeneities (Ishii and Tromp 1999; Lau et al. 2017) and basalt-rich slabs near the core-mantle boundary (e.g.Grand 2002). In addition, the very deep lower mantle has been suggested to host mixed-valence bridgmanite, even under reduced conditions in contact with metallic iron from the outer core (Shim et al. 2017). Regions rich in subducted basalt will have higher Al- and Si-content, which is more likely to stabilize mixed-valence iron in the bridgmanite A-site. Basalt graveyards could thus more efficiently conduct heat from the outer core, with corresponding effects on the formation of thermochemical plumes and entrainment of subducted material. As the densest heterogeneities identified in the lower mantle, ULVZs resting on the core-mantle boundary are likely Fe-rich (e.g. Rost et al. 2005; Brown et al. 2015), but their redox states are not well-constrained by available geophysical data. Proposed compositions for ULVZs include enrichment in metallic melt (Williams and Garnero 1996; Liu et al. 2016) or iron-rich oxide (Wicks et al. 2010; Hu et al. 2016; Liu et al. 2017) or silicate (Mao et al. 2006). However, the

high temperatures expected at the base of the mantle may impede charge transfer (Mattson and Rossman 1987, Xu and McCammon 2002), and additional mechanisms such as conductivity of vacancies and ions will be increasingly important at high temperatures (Xu and McCammon 2002). Future experimental studies will also need to quantify charge transfer in lower-mantle post-perovskite. If observed, enhanced electrical and thermal conductivity of ULVZs may indicate either the presence of Fe metal or charge transfer due to mixed-valence Fe-rich bridgmanite. Distinguishing these hypotheses is important to constraining redox evolution at the core-mantle boundary.

Acknowledgements

The authors thank Susanne Seitz for assistance with microprobe analysis of starting materials at the University of Lausanne. We thank Richard Gaal for assistance with gas loading at the EPFL and Sergey Tkachev for assistance at the APS. Use of the COMPRES-GSECARS gas loading system and the APS offline Mössbauer laboratory facilities was supported by COMPRES under NSF Cooperative Agreement EAR-1606856 and by GSECARS through NSF grant EAR-1634415 and DOE grant DE-FG02-94ER14466. ^{57}Co-source Mössbauer spectroscopy was performed at the APS beamline 3-ID Mössbauer Laboratory. This research used resources of the Advanced Photon Source, a U.S. Department of Energy (DOE) Office of Science User Facility operated for the DOE Office of Science by Argonne National Laboratory under Contract No. DE-AC02-06CH11357. We thank the European Synchrotron Radiation Facility (Grenoble, France) for provision of synchrotron radiation at beamlines ID18 for synchrotron Mössbauer spectroscopy, and beamlines ID09 and ID27 for synchrotron X-ray diffraction. Laser heating was performed at beamline ID24 of the ESRF with assistance from Innokenty Kantor. S. M. Dorfman

387 acknowledges funding support from the Marie Heim-Vögtlin program of the Swiss National
388 Science Foundation through project PMPDP2_151256 and the National Science Foundation
389 project EAR-1664332.

390 Figure and table captions

391 Figure 1: X-ray diffraction patterns for bridgmanites obtained after laser heating and before
392 decompression with energy-domain SMS, with diffraction angle converted to lattice spacing (d)
393 to account for differences in diffraction wavelength. Diffraction peaks from medium (N=NaCl,
394 and Ar for En90Hem10 sample) and minor stishovite (St) are identified, and black sticks below
395 comprise bridgmanite reference pattern.

396 Figure 2: Observed Mössbauer spectra at 1 bar. For compositions in a) b) and c), synchrotron
397 Mössbauer spectra are obtained at ESRF ID18 from iron-bearing bridgmanite samples recovered
398 to 1 bar after 300 K decompression from high-pressure synthesis. In d), conventional ^{57}Co
399 Mössbauer spectrum is obtained at APS sector 3 offline lab from synthetic akimotoite before 300
400 K compression. Blue doublets=Fe^{2+}. Red doublets=high spin Fe^{3+}. Purple doublets=$Fe^{2.5+}$ charge
401 transfer component. Original data are black points, with total fit indicated by red curve and misfit
402 by red points.

403 Figure 3: Observed Mössbauer spectra for iron-bearing bridgmanite at high pressure ~27 GPa
404 below the spin transition in Fe^{3+}. Spectra shown in a) b) and c) use synchrotron Mössbauer
405 source at ESRF ID18 (total Fe^{3+}/total Fe listed for each composition is assumed to be same as 1
406 bar recovered sample), while d) uses conventional ^{57}Co Mössbauer source at APS sector 3
407 offline lab. Blue doublets=Fe^{2+} (where darker blue indicates distorted A-site with high QS, and

lighter blue Fe^{2+} in untransformed glass in En90Hem10 composition in c)). Red doublets=high spin Fe^{3+}. Purple doublets=$Fe^{2.5+}$ charge transfer component. Original data are black points, with total fit indicated by red curve and misfit by red points.

Figure 4: Observed Mössbauer spectra for iron-bearing bridgmanite at high pressure ~72 GPa above the spin transition in Fe^{3+}. Spectra shown in a) b) and c) use synchrotron Mössbauer source at ESRF ID18 (total Fe^{3+}/total Fe listed for each composition is assumed to be same as 1 bar recovered sample), while d) uses conventional ^{57}Co Mössbauer source at APS sector 3 offline lab. Blue doublets=Fe^{2+} (where darker blue indicates distorted A-site with high QS, and lighter blue Fe^{2+} in untransformed glass in En90Hem10 composition in c)). Red doublets=high spin Fe^{3+}, and pink=low spin Fe^{3+}. Purple doublets=$Fe^{2.5+}$ charge transfer component. Original data are black points, with total fit indicated by red curve and misfit by red points.

Figure 5: Mössbauer parameters a) quadrupole splitting (QS) and b) center shift (CS) observed for bridgmanite as a function of pressure for all sites in all compositions. Symbols indicate bulk composition of each bridgmanite sample (diamonds: Fs75Co25, squares: En50Fs50, circles: En90Hem10, triangles: En50Hem10), while colors indicate spin and valence state of iron (blue: Fe^{2+}, purple: $Fe^{2.5+}$ (charge transfer), red: high-spin Fe^{3+}, light pink: low-spin Fe^{3+}, magenta: mixed-spin Fe^{3+} (overlap between doublets impedes resolution of separate high- and low-spin doublets).

Figure 6: a) Relative total amount of high-spin iron in each sample as a function of pressure, based on sum of area of all high-spin Fe^{2+}, $Fe^{2.5+}$, and Fe^{3+} doublets. b) Relative total amount of Fe^{3+} in each sample as a function of pressure, based on area of Fe^{3+} doublets plus half the area of

charge transfer component. Error bars represent 2σ obtained from fit of Mössbauer spectral intensity.

Figure 7: Mössbauer parameters observed for Fe in bridgmanite and other compounds. Results from this study for Fe^{2+}=blue circles, high-spin Fe^{3+}=red up-pointing triangles, low-spin Fe^{3+}=pink down-pointing triangles, charge transfer ($Fe^{2.5+}$) component=purple diamonds. Error bars represent fit uncertainty for each doublet. Predicted values for QS from density functional theory for Fe^{2+} from (Hsu et al. 2010) and for Fe^{3+} from (Hsu et al. 2011). Shaded regions comprise envelope of observations from previous studies: (Greenwood and Gibb 1971; Pasternak et al. 2002; Hummer and Fei 2012; McCammon et al. 2013).

Table 1: Microprobe composition analysis of starting materials performed at the University of Lausanne. Standards used to quantify SiO_2, MgO, and FeO were forsterite, fayalite and orthopyroxene. Oxide totals for glass were consistently less than 100%, potentially due to use of Fe^{2+}-rich standards, higher Fe^{3+}-content in glass, and matrix effects. Measurements with totals less than 97% were dropped. FeO vs. $FeO_{1.5}$ was determined by Mössbauer spectroscopy at ambient conditions.

Table 2: Mössbauer parameters observed for bridgmanite. CS and QS in units of mm/s. * indicates parameters constrained to equal values to aid fit convergence. Note that $Fe^{2.5+}$ fraction can be assumed to represent 50% Fe^{2+} + 50% Fe^{3+}.

Table 3: Hyperfine parameters of high- and low-spin Fe^{3+} in perovskites obtained by energy-domain Mössbauer spectroscopy.

Tables and figures

Table 1

	En50Fs50 (pigeonite)		En90Hem10 (glass)	
	Weight % oxides	Cations normalized to 3 O (3% Fe^{3+})	Weight % oxides	Cations normalized to 3 O (30% Fe^{3+})
SiO_2	52.0(2)	0.996	49.2(2)	0.900
MgO	18.1(2)	0.519	35.4(4)	0.965
FeO	30.3(2)	0.478	13.31(18)	0.143
$FeO_{1.5}$		0.015		0.061
Total	100.4(4)	1.993	97.8(6)	2.069

452 Table 2

	Fs75Co25			En50Fs50			
	1 bar			1 bar			
	Fe^{2+}		$Fe^{2.5+}$	Fe^{2+}		Fe^{3+} HS	
CS (mm/s)	1.07(4)		0.60(8)	1.06(3)		0.39(3)	
QS (mm/s)	2.01(7)		1.06(20)	1.96(6)		0	
Weight	80(11)		20(11)	72(6)		28(6)	
	15 GPa			25 GPa			
	Fe^{2+}		$Fe^{2.5+}$	Fe^{2+}		Fe^{3+} HS	
CS	1.089* (18)	1.089* (18)	0.84(15)	1.21(5)	1.08(3)	0.2(3)	
QS	3.66(8)	2.34(2)	1.2(3)	2.69(11)	1.73(9)	1.0(4)	
Weight	6(9)	76(17)	17(16)	52(27)	26(21)	22(21)	
	76 GPa			75 GPa			
	Fe^{2+}		$Fe^{2.5+}$	Fe^{2+}		$Fe^{2.5+}$	Fe^{3+} HS
CS	0.998(9)	1.0(3)	0.6(2)	0.985(8)	1.00(4)	0.9(9)	0.4 (10)
QS	3.926 (19)	2.4(4)	1.7(7)	3.90(2)	3.1(3)	1.6 (1.9)	0.7 (19)
Weight	28(14)	54(20)	18(19)	20(27)	43(28)	18(17)	18(18)
	En90Hem10			En50Hem50			
	1 bar			1 bar			
	Fe^{2+}		Fe^{3+} HS	Fe^{3+} HS			
CS	1.02(7)		0.42(9)	0.36(3)			
QS	1.96(19)		0.95(16)	0.73(5)			
Weight	47(9)		53(9)	100			
	36 GPa			32 GPa			
	Fe^{2+}		Fe^{3+} HS	Fe^{3+} A HS		Fe^{3+} B HS	
CS	1.2(8)	0.8(7)	0.34(3)	0.35(2)		0.32(3)	
QS	3.1(1.7)	2.3(1.4)	1.02(6)	1.37(11)		0.59(10)	
Weight	22(14)	25(18)	52(16)	0.5*		0.5*	
	67 GPa			70 GPa			
	Fe^{2+}		Fe^{3+} mixed	Fe^{3+} A HS		Fe^{3+} B LS	
CS	1.0(3)	0.81(13)	0.29(3)	0.38(9)		-0.07(10)	
QS	3.3(3)	2.3(7)	1.13(9)	1.35(4)		1.30(5)	
Weight	20(17)	31(16)	50(15)	0.5*		0.5*	

453

454

455 Table 3

	HS CS (mm/s)	HS QS (mm/s)	LS CS (mm/s)	LS QS (mm/s)	Reference
Bridgmanite $(Mg,Fe,Al)(Fe,Al,Si)O_3$	0.0-0.5	0.3-1.7	N/A	N/A	(Hummer and Fei 2012)
	0.4	1.2-1.5	N/A	N/A	(Potapkin et al. 2013)
	0.4	0.8-1.3	-0.1	0.9	(Kupenko et al. 2015)
	0.1-0.15 (ΔIS A-B)	1.1-1.2	0.3 (ΔIS A-B)	1.3-1.4	(Liu et al. 2018)
	0.2-0.4	0.6-1.4	0.0	1.3	This work
Perovskite-structured rare-earth orthoferrites	0.22-0.24	0.24-0.59	0.04-0.23	0.55-1.42	(Pasternak et al. 2002)

456

457

458 Figure 1

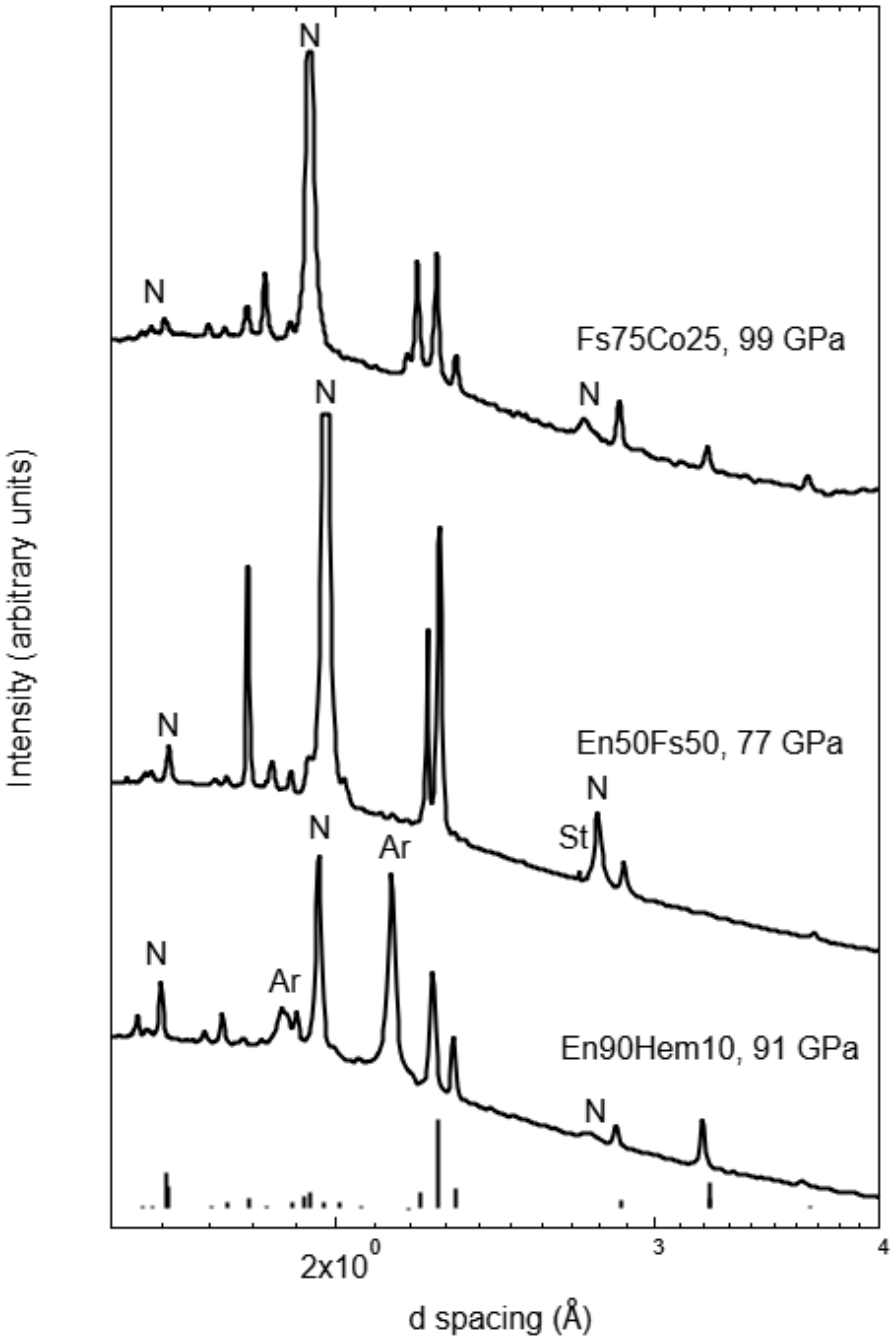

459

460 Figure 2

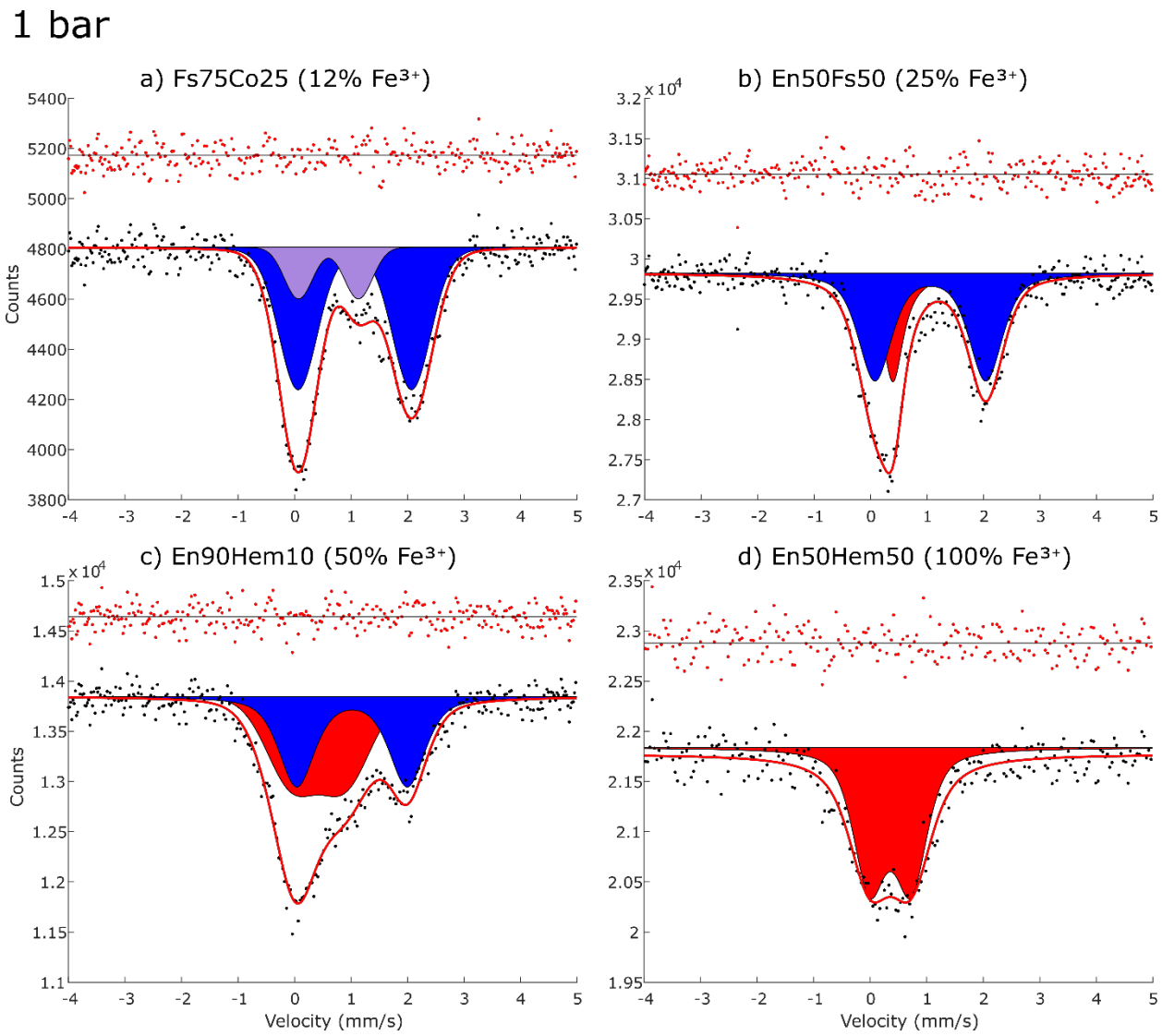

461

462 Figure 3

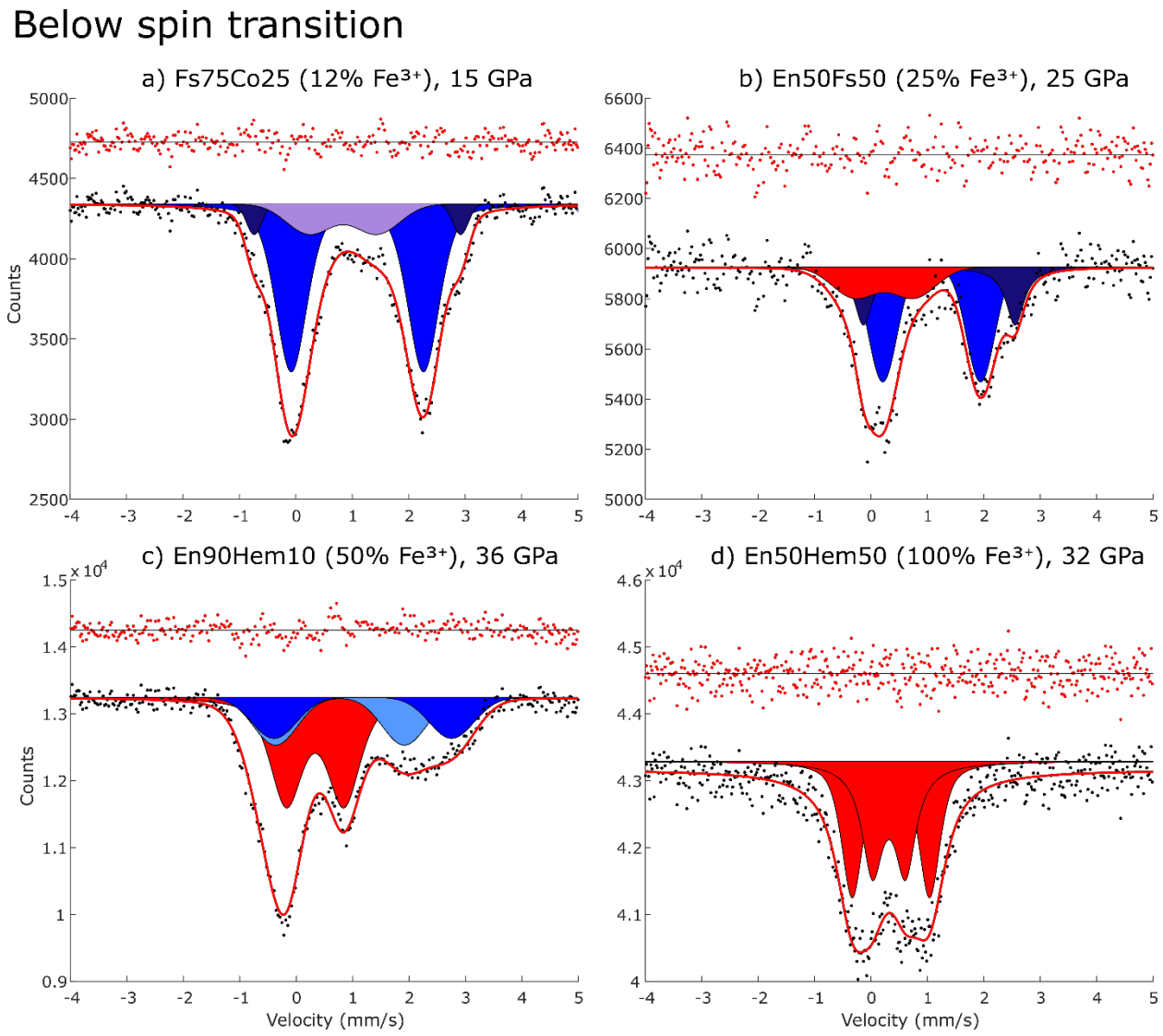

463

464

465 Figure 4

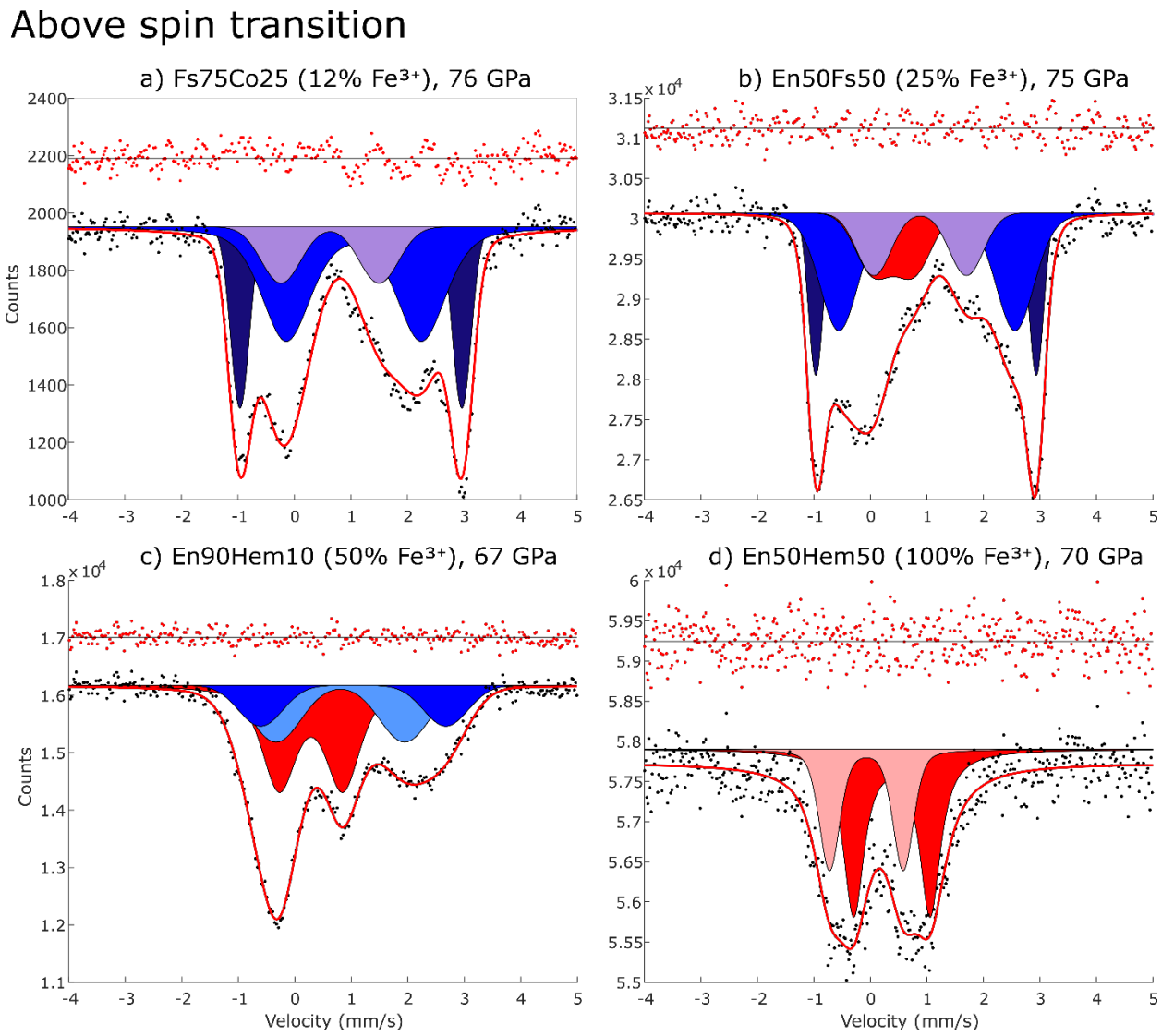

466

467

468

469

Figure 5

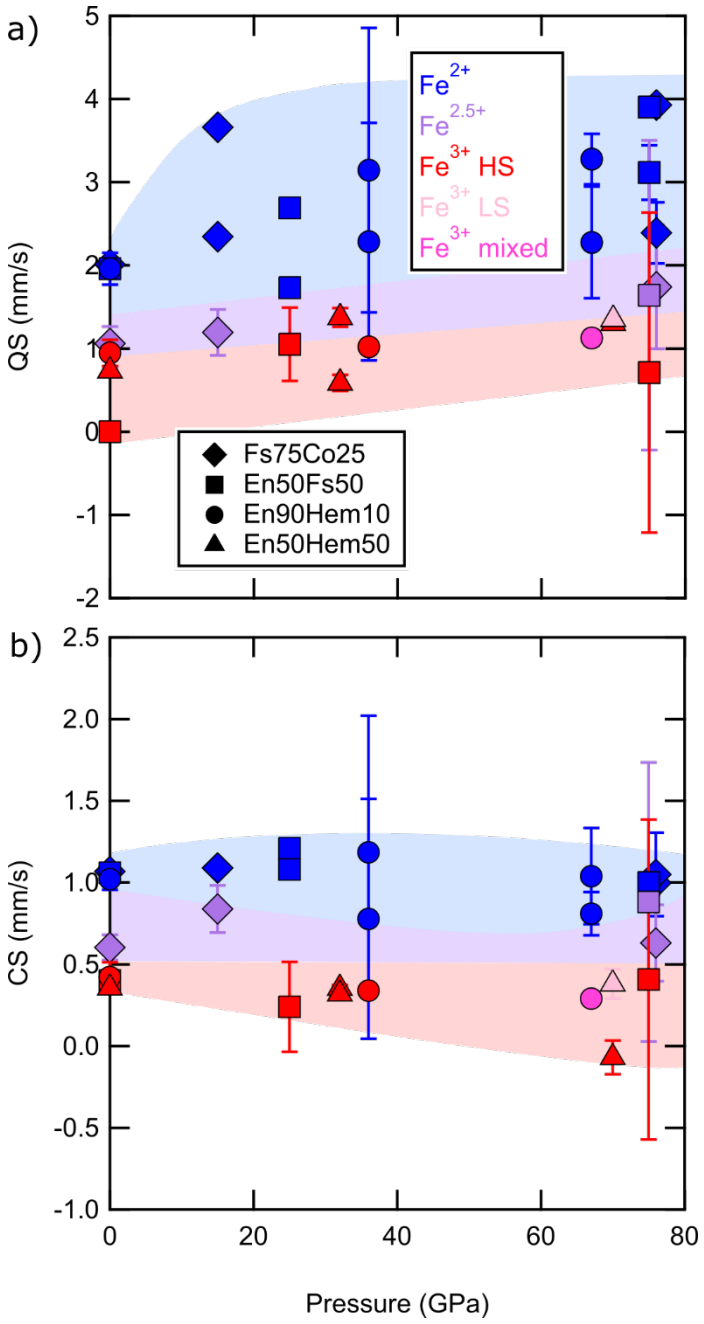
a)
b)
QS (mm/s)
CS (mm/s)
Pressure (GPa)
Fe2+
Fe2.5+
Fe3+ HS
Fe3+ LS
Fe3+ mixed
Fs75Co25
En50Fs50
En90Hem10
En50Hem50

472 Figure 6

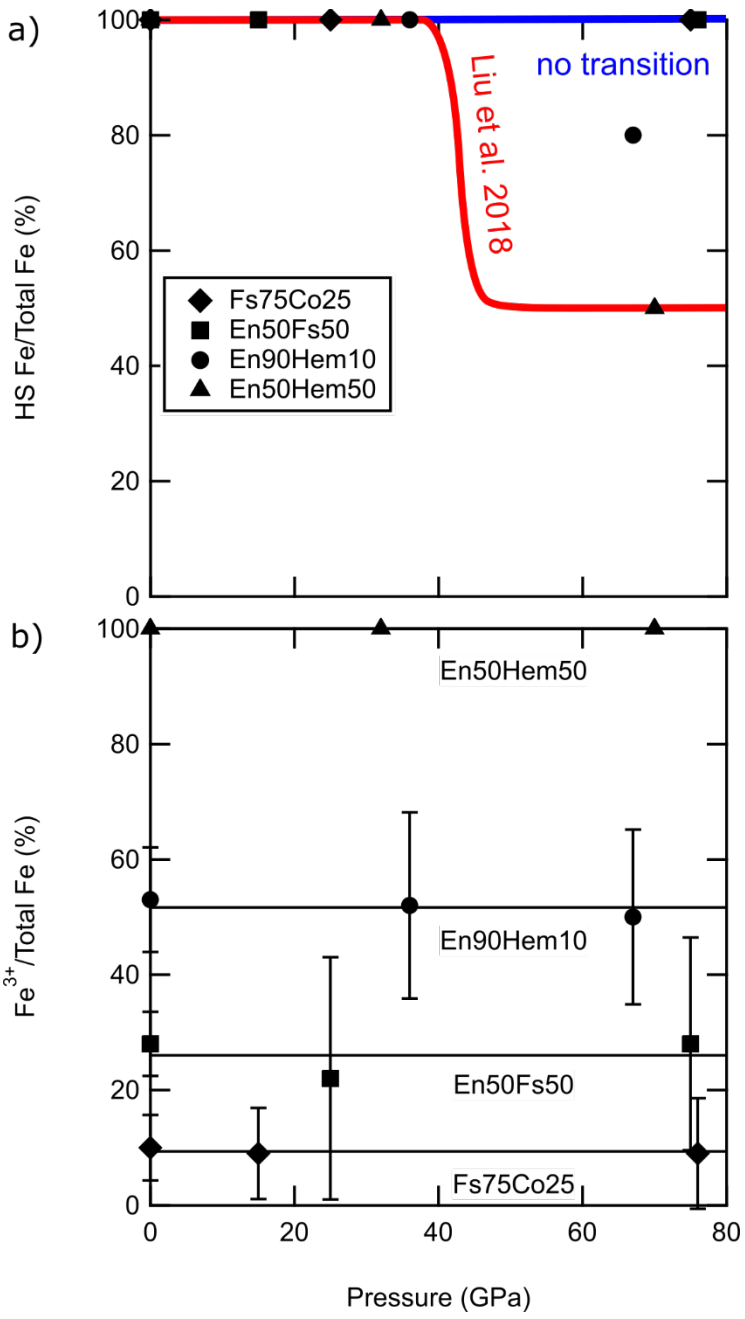

473

474

475

476 Figure 7

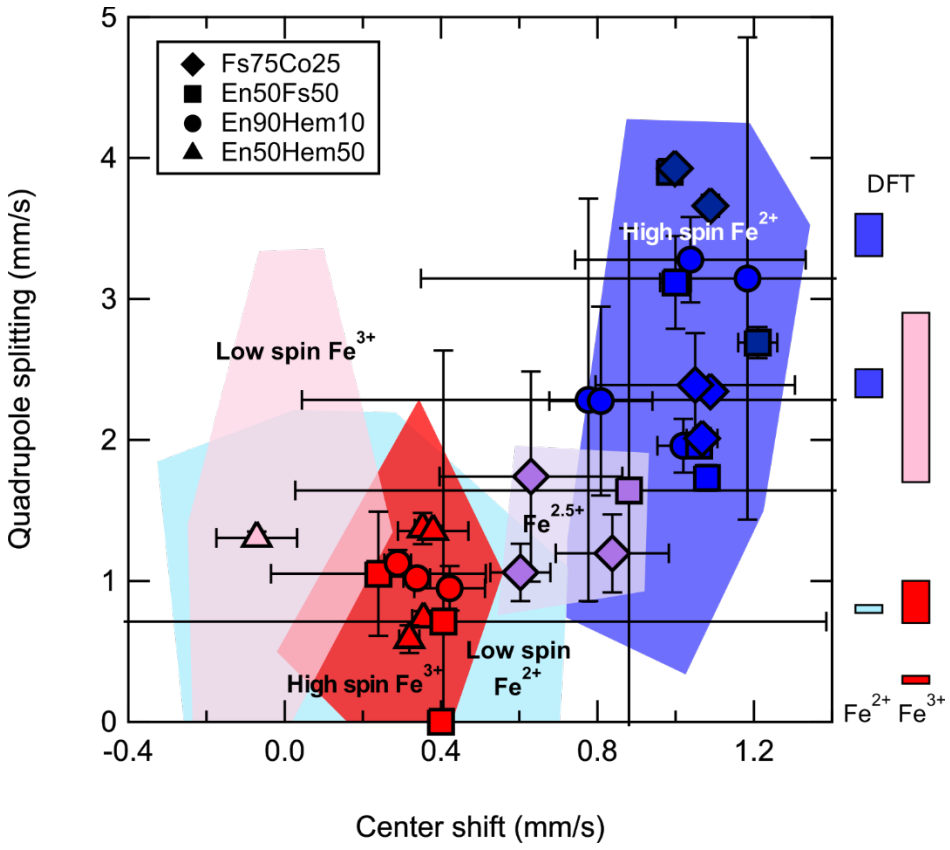

477

478

References

Akahama, Y., and Kawamura, H. (2006) Pressure calibration of diamond anvil Raman gauge to 310 GPa. Journal of Applied Physics, 100, 043516–4.

Badro, J. (2014) Spin Transitions in Mantle Minerals. Annual Review of Earth and Planetary Sciences, 42, 231–248.

Badro, J., Rueff, J.-P., Vanko, G., Monaco, G., Fiquet, G., and Guyot, F. (2004) Electronic Transitions in Perovskite: Possible Nonconvecting Layers in the Lower Mantle. Science, 305, 383–386.

Brown, S.P., Thorne, M.S., Miyagi, L., and Rost, S. (2015) A compositional origin to ultralow-velocity zones. Geophysical Research Letters, 2014GL062097.

Burns, R.G. (1993) Mineralogical Applications of Crystal Field Theory, 563 p. Cambridge University Press.

Caracas, R. (2010) Spin and structural transitions in $AlFeO_3$ and $FeAlO_3$ perovskite and post-perovskite. Physics of the Earth and Planetary Interiors.

Catalli, K., Shim, S.-H., Prakapenka, V.B., Zhao, J., Sturhahn, W., Chow, P., Xiao, Y., Liu, H., Cynn, H., and Evans, W.J. (2010) Spin state of ferric iron in $MgSiO_3$ perovskite and its effect on elastic properties. Earth and Planetary Science Letters, 289, 68–75.

Catalli, K., Shim, S.-H., Dera, P., Prakapenka, V.B., Zhao, J., Sturhahn, W., Chow, P., Xiao, Y., Cynn, H., and Evans, W.J. (2011) Effects of the Fe^{3+} spin transition on the properties of aluminous perovskite—New insights for lower-mantle seismic heterogeneities. Earth and Planetary Science Letters, 310, 293–302.

Dorfman, S.M., and Duffy, T.S. (2014) Effect of Fe-enrichment on seismic properties of perovskite and post-perovskite in the deep lower mantle. Geophysical Journal International, 197, 910–919.

Dorfman, S.M., Shieh, S.R., Meng, Y., Prakapenka, V.B., and Duffy, T.S. (2012) Synthesis and equation of state of perovskites in the $(Mg, Fe)_3Al_2Si_3O_{12}$ system to 177 GPa. Earth and Planetary Science Letters, 357–358, 194–202.

Dorfman, S.M., Meng, Y., Prakapenka, V.B., and Duffy, T.S. (2013) Effects of Fe-enrichment on the equation of state and stability of $(Mg,Fe)SiO_3$ perovskite. Earth and Planetary Science Letters, 361, 249–257.

Dorfman, S.M., Dutton, S.E., Potapkin, V., Chumakov, A., Rueff, J.-P., Chow, P., Xiao, Y., Cava, R.J., Duffy, T.S., McCammon, C.A., and others (2016) Electronic transitions of iron in almandine-composition glass to 91 GPa. American Mineralogist, 101.

512 Dyar, M.D., Agresti, D.G., Schaefer, M.W., Grant, C.A., and Sklute, E.C. (2006) Mössbauer
513 spectroscopy of Earth and planetary materials. Annual Review of Earth and Planetary
514 Sciences, 34, 83–125.

515 Fei, Y., Virgo, D., Mysen, B.O., Wang, Y., and Mao, H. -k. (1994) Temperature-dependent
516 electron delocalization in (Mg,Fe)SiO3 perovskite. American Mineralogist, 79, 826–837.

517 Fei, Y., Wang, Y., and Finger, L.W. (1996) Maximum solubility of FeO in (Mg,Fe)SiO_3-
518 perovskite as a function of temperature at 26 GPa: Implication for FeO content in the
519 lower mantle. Journal of Geophysical Research, 101, 11525–11530.

520 Frost, D.J., and Langenhorst, F. (2002) The effect of Al_2O_3 on Fe–Mg partitioning between
521 magnesiowüstite and magnesium silicate perovskite. Earth and Planetary Science Letters,
522 199, 227–241.

523 Frost, D.J., and McCammon, C.A. (2008) The redox state of Earth's mantle. Annual Review of
524 Earth and Planetary Sciences, 36, 389–420.

525 Frost, D.J., Liebske, C., Langenhorst, F., McCammon, C.A., Trønnes, R.G., and Rubie, D.C.
526 (2004) Experimental evidence for the existence of iron-rich metal in the Earth's lower
527 mantle. Nature, 428, 409–412.

528 Grand, S.P. (2002) Mantle Shear–Wave Tomography and the Fate of Subducted Slabs.
529 Philosophical Transactions of the Royal Society of London A, 360, 2475–91.

530 Greenwood, N.N., and Gibb, T.C. (1971) Low-spin Iron(II) and Iron(III) Complexes. In
531 Mössbauer Spectroscopy pp. 169–193. Springer Netherlands.

532 Grüninger, H., Liu, Z., Siegel, R., Ballaran, T.B., Katsura, T., Senker, J., and Frost, D.J. (2019)
533 Oxygen Vacancy Ordering in Aluminous Bridgmanite in the Earth's Lower Mantle.
534 Geophysical Research Letters, 46, 8731–8740.

535 Gu, C., Catalli, K., Grocholski, B., Gao, L., Alp, E., Chow, P., Xiao, Y., Cynn, H., Evans, W.J.,
536 and Shim, S.-H. (2012) Electronic structure of iron in magnesium silicate glasses at high
537 pressure. Geophysical Research Letters, 39.

538 Gu, T., Li, M., McCammon, C., and Lee, K.K.M. (2016) Redox-induced lower mantle density
539 contrast and effect on mantle structure and primitive oxygen. Nature Geoscience, 9, 723–
540 727.

541 Hsu, H., Umemoto, K., Blaha, P., and Wentzcovitch, R.M. (2010) Spin states and hyperfine
542 interactions of iron in (Mg,Fe)SiO_3 perovskite under pressure. Earth and Planetary
543 Science Letters, 294, 19–26.

Hsu, H., Blaha, P., Cococcioni, M., and Wentzcovitch, R.M. (2011) Spin-State Crossover and Hyperfine Interactions of Ferric Iron in $MgSiO_3$ Perovskite. Physical Review Letters, 106, 118501.

Hu, Q., Kim, D.Y., Yang, W., Yang, L., Meng, Y., Zhang, L., and Mao, H.-K. (2016) FeO_2 and FeOOH under deep lower-mantle conditions and Earth's oxygen–hydrogen cycles. Nature, 534, 241–244.

Hummer, D.R., and Fei, Y. (2012) Synthesis and crystal chemistry of Fe3+-bearing (Mg,Fe3+)(Si,Fe3+)O3 perovskite. American Mineralogist, 97, 1915–1921.

Ishii, M., and Tromp, J. (1999) Normal-Mode and Free-Air Gravity Constraints on Lateral Variations in Velocity and Density of Earth's Mantle. Science, 285, 1231–1236.

Ismailova, L., Bykova, E., Bykov, M., Cerantola, V., McCammon, C., Ballaran, T.B., Bobrov, A., Sinmyo, R., Dubrovinskaia, N., Glazyrin, K., and others (2016) Stability of Fe,Al-bearing bridgmanite in the lower mantle and synthesis of pure Fe-bridgmanite. Science Advances, 2, e1600427.

Jackson, J.M., Sturhahn, W., Shen, G., Zhao, J., Hu, M.Y., Errandonea, D., Bass, J.D., and Fei, Y. (2005) A synchrotron Mössbauer spectroscopy study of $(Mg,Fe)SiO_3$ perovskite up to 120 GPa. American Mineralogist, 90, 199–205.

Keppler, H., Dubrovinsky, L.S., Narygina, O., and Kantor, I. (2008) Optical Absorption and Radiative Thermal Conductivity of Silicate Perovskite to 125 Gigapascals. Science, 322, 1529–1532.

Kupenko, I., McCammon, C.A., Sinmyo, R., Cerantola, V., Potapkin, V., Chumakov, A.I., Kantor, A.P., Rüffer, R., and Dubrovinsky, L.S. (2015) Oxidation state of the lower mantle: In situ observations of the iron electronic configuration in bridgmanite at extreme conditions. Earth and Planetary Science Letters, 423, 78–86.

Lau, H.C.P., Mitrovica, J.X., Davis, J.L., Tromp, J., Yang, H.-Y., and Al-Attar, D. (2017) Tidal tomography constrains Earth's deep-mantle buoyancy. Nature, 551, 321–326.

Lin, J.-F., Speziale, S., Mao, Z., and Marquardt, H. (2013) Effects of the electronic spin transitions of iron in lower mantle minerals: Implications for deep mantle geophysics and geochemistry. Reviews of Geophysics, 51.

Liu, J., Li, J., Hrubiak, R., and Smith, J.S. (2016) Origins of ultralow velocity zones through slab-derived metallic melt. Proceedings of the National Academy of Sciences, 113, 5547–5551.

Liu, J., Hu, Q., Kim, D.Y., Wu, Z., Wang, W., Xiao, Y., Chow, P., Meng, Y., Prakapenka, V.B., Mao, H.-K., and others (2017) Hydrogen-bearing iron peroxide and the origin of ultralow-velocity zones. Nature, 551, 494.

Liu, J., Dorfman, S.M., Zhu, F., Li, J., Wang, Y., Zhang, D., Xiao, Y., Bi, W., and Alp, E.E. (2018) Valence and spin states of iron are invisible in Earth's lower mantle. Nature Communications, 9, 1284.

Liu, Z., Boffa Ballaran, T., Huang, R., Frost, D.J., and Katsura, T. (2019) Strong correlation of oxygen vacancies in bridgmanite with Mg/Si ratio. Earth and Planetary Science Letters, 523, 115697.

Lobanov, S.S., Holtgrewe, N., Lin, J.-F., and Goncharov, A.F. (2017) Radiative conductivity and abundance of post-perovskite in the lowermost mantle. Earth and Planetary Science Letters, 479, 43–49.

Long, Y.W., Hayashi, N., Saito, T., Azuma, M., Muranaka, S., and Shimakawa, Y. (2009) Temperature-induced A–B intersite charge transfer in an A-site-ordered LaCu3Fe4O12 perovskite. Nature, 458, 60–63.

Mao, H. -k., Xu, J., and Bell, P.M. (1986) Calibration of the Ruby Pressure Gauge to 800 kbar Under Quasi-Hydrostatic Conditions. Journal of Geophysical Research, 91, 4673–4676.

Mao, W.L., Mao, H., Sturhahn, W., Zhao, J., Prakapenka, V.B., Meng, Y., Shu, J., Fei, Y., and Hemley, R.J. (2006) Iron-rich post-perovskite and the origin of ultralow-velocity zones. Science, 312, 564–565.

Mao, Z., Lin, J.-F., Yang, J., Inoue, T., and Prakapenka, V.B. (2015) Effects of the Fe3+ spin transition on the equation of state of bridgmanite. Geophysical Research Letters, 42, 2015GL064400.

Mattson, S.M., and Rossman, G.R. (1987) Identifying characteristics of charge transfer transitions in minerals. Physics and Chemistry of Minerals, 14, 94–99.

McCammon, C., Glazyrin, K., Kantor, A., Kantor, I., Kupenko, I., Narygina, O., Potapkin, V., Prescher, C., Sinmyo, R., Chumakov, A., and others (2013) Iron spin state in silicate perovskite at conditions of the Earth's deep interior. High Pressure Research, 0, 1–10.

Pasternak, M.P., Xu, W.M., Rozenberg, G.Kh., and Taylor, R.D. (2002) Electronic, Magnetic and Structural Properties of the $RFeO_3$ Antiferromagnetic-Perovskites at Very High Pressures. In Symposium D – Perovskite Materials Vol. 718.

Piet, H., Badro, J., Nabiei, F., Dennenwaldt, T., Shim, S.-H., Cantoni, M., Hébert, C., and Gillet, P. (2016) Spin and valence dependence of iron partitioning in Earth's deep mantle. Proceedings of the National Academy of Sciences, 201605290.

Potapkin, V., Chumakov, A.I., Smirnov, G.V., Celse, J.-P., Rüffer, R., McCammon, C., and Dubrovinsky, L. (2012) The ^{57}Fe Synchrotron Mössbauer Source at the ESRF. Journal of Synchrotron Radiation, 19, 559–569.

Potapkin, V., McCammon, C.A., Glazyrin, K.D., Kantor, A.P., Kupenko, I., Prescher, C., Sinmyo, R., Smirnov, G.V., Chumakov, A.I., Rüffer, R., and others (2013) Effect of iron oxidation state on the electrical conductivity of the Earth's lower mantle. Nature Communications, 4, 1427.

Prescher, C., McCammon, C., and Dubrovinsky, L. (2012) MossA: a program for analyzing energy-domain Mössbauer spectra from conventional and synchrotron sources. Journal of Applied Crystallography, 45, 329–331.

Prescher, C., Weigel, C., McCammon, C.A., Narygina, O., Potapkin, V., Kupenko, I., Sinmyo, R., Chumakov, A.I., and Dubrovinsky, L.S. (2014) Iron spin state in silicate glass at high pressure: Implications for melts in the Earth's lower mantle. Earth and Planetary Science Letters, 385, 130–136.

Ricolleau, A., Fei, Y., Cottrell, E., Watson, H., Deng, L., Zhang, L., Fiquet, G., Auzende, A.-L., Roskosz, M., Morard, G., and others (2009) Density profile of pyrolite under the lower mantle conditions. Geophysical Research Letters, 36, L06302.

Rivers, M., Prakapenka, V., Kubo, A., Pullins, C., Holl, C.M., and Jacobsen, S.D. (2008) The COMPRES/GSECARS gas-loading system for diamond anvil cells at the Advanced Photon Source. High Pressure Research, 28, 273–292.

Rost, S., Garnero, E.J., Williams, Q., and Manga, M. (2005) Seismological constraints on a possible plume root at the core-mantle boundary. Nature, 435, 666–669.

Rüffer, R., and Chumakov, A.I. (1996) Nuclear Resonance Beamline at ESRF. Hyperfine Interactions, 97–98, 589–604.

Shim, S.-H., Grocholski, B., Ye, Y., Alp, E.E., Xu, S., Morgan, D., Meng, Y., and Prakapenka, V.B. (2017) Stability of ferrous-iron-rich bridgmanite under reducing midmantle conditions. Proceedings of the National Academy of Sciences, 201614036.

Shukla, G., Cococcioni, M., and Wentzcovitch, R.M. (2016) Thermoelasticity of Fe3+- and Al-bearing bridgmanite: Effects of iron spin crossover. Geophysical Research Letters, 43, 5661–5670.

Sinmyo, R., Pesce, G., Greenberg, E., McCammon, C., and Dubrovinsky, L. (2014) Lower mantle electrical conductivity based on measurements of Al, Fe-bearing perovskite under lower mantle conditions. Earth and Planetary Science Letters, 393, 165–172.

Tange, Y., Takahashi, E., Nishihara, Y., Funakoshi, K., and Sata, N. (2009) Phase relations in the system MgO-FeO-SiO_2 to 50 GPa and 2000°C: An application of experimental techniques using multianvil apparatus with sintered diamond anvils. Journal of Geophysical Research, 114, B02214.

Tateno, S., Hirose, K., Sata, N., and Ohishi, Y. (2007) Solubility of FeO in (Mg,Fe)SiO_3 perovskite and the post-perovskite phase transition. Physics of the Earth and Planetary Interiors, 160, 319–325.

Weber, J.K.R., Hampton, D.S., Merkley, D.R., Rey, C.A., Zatarski, M.M., and Nordine, P.C. (1994) Aero-acoustic levitation: A method for containerless liquid-phase processing at high temperatures. Review of Scientific Instruments, 65, 456–465.

Wicks, J.K., Jackson, J.M., and Sturhahn, W. (2010) Very low sound velocities in iron-rich (Mg,Fe)O: Implications for the core-mantle boundary region. Geophysical Research Letters, 37, 5 PP.

Williams, Q., and Garnero, E.J. (1996) Seismic Evidence for Partial Melt at the Base of Earth's Mantle. Science, 273, 1528–1530.

Xu, Y., and McCammon, C.A. (2002) Evidence for ionic conductivity in lower mantle (Mg,Fe)(Si,Al)O_3 perovskite. Journal of Geophysical Research, 107.